INTERNATIONAL JOURNAL FOR NUMERICAL METHODS IN FLUIDS
Int. J. Numer. Meth. Fluids 2007; **54**:313–324
Published online 28 November 2006 in Wiley InterScience (www.interscience.wiley.com). DOI: 10.1002/fld.1400

Numerical study of hysteresis in annular swirling jets with a stepped-conical nozzle

M. Vanierschot*,† and E. Van den Bulck

Mechanical Engineering Department, K.U. Leuven, Heverlee, Belgium

SUMMARY

This study investigates the experimentally observed hysteresis in the mean flow field of an annular swirling jet with a stepped-conical nozzle. The flow is simulated using the Reynolds-averaged Navier–Stokes (RANS) approach for incompressible flow with a k–ε and a Reynolds stress transport (RSTM) turbulence model. Four different flow structures are observed depending on the swirl number: 'closed jet flow', 'open jet flow low swirl', 'open jet flow high swirl' and 'coanda jet flow'. These flow patterns change with varying swirl number and hysteresis at low and intermediate swirl numbers is revealed when increasing and subsequently decreasing the swirl. The influence of the inlet velocity profile on the transitional swirl numbers is investigated. When comparing computational fluid dynamics with experiments, the results show that both turbulence models predict the four different flow structures and the associated hysteresis and multiple solutions at low and intermediate swirl numbers. Therefore, a good agreement exists between experiments and numerics. Copyright © 2006 John Wiley & Sons, Ltd.

Received 3 April 2006; Revised 3 October 2006; Accepted 5 October 2006

KEY WORDS: annular swirling flow; free jet; stepped-conical nozzle; hysteresis

1. INTRODUCTION

Swirling flows have been widely studied over the past few decades. They have a broad range of applications varying from flame stabilization and enhanced mixing in combustion to separating particles from a flow in cyclone separators [1]. Swirl can significantly change the axial and radial velocity fields of an axisymmetric flow. These changes make it possible to create different flow structures in the same geometry by changing the swirl number [2, 3]. A numerical study of two such different flow structures is presented by Jiang and Shen [4]. They report on two

*Correspondence to: M. Vanierschot, Department of Mechanical Engineering, Division TME, Celestijnenlaan 300 A, Heverlee B-3001, Belgium.
†E-mail: Maarten.Vanierschot@mech.kuleuven.be

different flow patterns which they call the low and the high swirl pattern. These patterns show a bifurcation between the increase and decrease of swirl. They suggest that the bifurcation is due to the interaction between the internal recirculation zone on the central axis and the external recirculation zone between the jet and the confinement. Only limited comparison with experiments is provided and indirect evidence of such an experimental bifurcation is suggested based upon the data reported by Sloan *et al*. [5].

In this study, numerical simulations of annular swirling flows at different swirl numbers are performed to predict the transitional swirl numbers, i.e. the swirl numbers at which the flow structure changes. Numerically predicting these transitional swirl numbers can be useful in designing nozzle geometries for cold flow applications as well for combustion replacing time consuming experimental studies, such as the one performed by Vanierschot and Van den Bulck [6]. The numerical calculations are validated with original experimental data [3]. Four different flow structures are identified depending on the swirl number. These flow structures also show hysteresis between the increase and subsequent decrease of swirl, numerical as well as experimental. Similar hysteresis in the flame patterns in an annular swirl combustor is reported by Vanoverberghe *et al*. [7]. They report five different flame patterns in a similar geometry as the one in this study. Hysteresis exists between the different flames depending on the history in swirl number and degree of premix.

2. NUMERICAL PROCEDURE

2.1. Governing equations

The governing equations that are used here to describe the steady state swirling flow are the Reynolds averaged Navier–Stokes equations in cylindrical co-ordinates. Due to the axisymmetry found in the experimental linear discriminant analysis (LDA) measurements, the mean flow is considered to be invariant in the azimuthal direction giving $\partial/\partial\theta = 0$. Therefore, the equations governing this type of flow for continuity and momentum may be written as

$$\frac{\partial \rho U}{\partial x} + \frac{1}{r}\frac{\rho r V}{\partial r} = 0 \tag{1}$$

$$\frac{\partial \rho r U \phi}{\partial x} + \frac{\partial \rho r V \phi}{\partial r} = \frac{\partial}{\partial x}\left(r\mu\frac{\partial \phi}{\partial x}\right) + \frac{\partial}{\partial r}\left(r\mu\frac{\partial \phi}{\partial r}\right) + r S_\phi \tag{2}$$

where U, V and W are the mean axial, radial and azimuthal velocities and ϕ stands for any of the momentum components U, V and rW. The source term for the momentum equation S_ϕ is defined as

$$S_U = -\frac{\partial P}{\partial x} - \frac{\partial \rho \overline{u^2}}{\partial x} - \frac{1}{r}\frac{\partial r \rho \overline{uv}}{\partial r} \tag{3}$$

$$S_V = -\frac{\partial P}{\partial r} + \frac{\rho W^2}{r} - \frac{\mu V}{r^2} - \frac{1}{r}\frac{\partial r \rho \overline{v^2}}{\partial r} + \frac{\rho \overline{w^2}}{r} - \frac{\partial \rho \overline{uv}}{\partial x} \tag{4}$$

$$S_{rW} = -\frac{2\mu}{r}\frac{\partial r W}{\partial r} - r\frac{\partial \rho \overline{uw}}{\partial x} - r\frac{\partial \rho \overline{vw}}{\partial r} - 2\rho \overline{vw} \tag{5}$$

DOI: 10.1002/fld

The Reynolds stresses $\overline{u^2}$, $\overline{v^2}$, $\overline{w^2}$, $\overline{uv}$, $\overline{uw}$ and $\overline{vw}$ are computed using two different approaches. The first approach is the standard k–ε turbulence model [8]. The Reynolds stresses are related to the mean velocity gradients by the Boussinesq hypothesis *via* the turbulent viscosity ν_t. This turbulent viscosity is calculated as $\nu_t = C_\mu k^2/\varepsilon$, where $C_\mu = 0.09$, k is the turbulent kinetic energy and ε is the turbulent dissipation rate. These quantities are calculated by solving two extra transport equations in combination with Equations (1) and (2). The second approach is solving the transport equations for the Reynolds stresses [9, 10]. These can be written as (in cartesian co-ordinates)

$$\frac{\partial}{\partial x_k}(\rho U_k \overline{u_i u_j}) - \frac{\partial}{\partial x_k}\left(\mu \frac{\partial \overline{u_i u_j}}{\partial x_k}\right) = P_{ij} - \frac{2}{3}\rho\delta_{ij}\varepsilon + D_{\mathrm{T},ij} + \phi_{ij} \tag{6}$$

where $P_{ij} = -\rho(\overline{u_i u_k}\partial U_j/\partial x_k + \overline{u_j u_k}\partial U_i/\partial x_k)$ is the production of the stress $\overline{u_i u_j}$, the dissipation ε is calculated by solving a transport equation, $D_{\mathrm{T},ij}$ is the turbulent diffusion and ϕ_{ij} is the pressure strain. The last two terms need to be modelled. The gradient-diffusion model for $D_{\mathrm{T},ij}$ of Daly and Harlow [11] can cause numerical instabilities and therefore a simplified version proposed by Lien and Leschziner [12] is used. The model used for ϕ_{ij} is the one proposed by Gibson and Launder [10].

2.2. *Computational domain*

A schematic view of the geometry and the computational domain is shown in Figure 1. Through the inlet, air enters an annular channel with outer radius $R_o = 43.5$ mm and inner radius $R_i = 0.65R_o$. A stepped-conical nozzle is placed at the outlet of the annular channel. This nozzle has a stepwise expansion with a height of $0.3R_o$, followed by a divergent of axial length $0.88R_o$ and opening angle $\alpha = 20°$. The nozzle is followed by a sudden expansion into a large confinement of radius $30R_o$. The outlet is chosen to be at $65R_o$. The x-axis of the cylindrical polar co-ordinate system (x, r, θ) is coincident with the central axis of the geometry and the origin is located at the exit of the annular channel, so the stepwise expansion begins at $x = 0$ mm. For the calculations, air is chosen as the working fluid with a density $\rho = 1.1708\,\mathrm{kg/m^3}$ and a kinematic viscosity $\nu = 1.85 \times 10^{-5}\,\mathrm{m^2/s}$. The fluid chosen is incompressible and Newtonian.

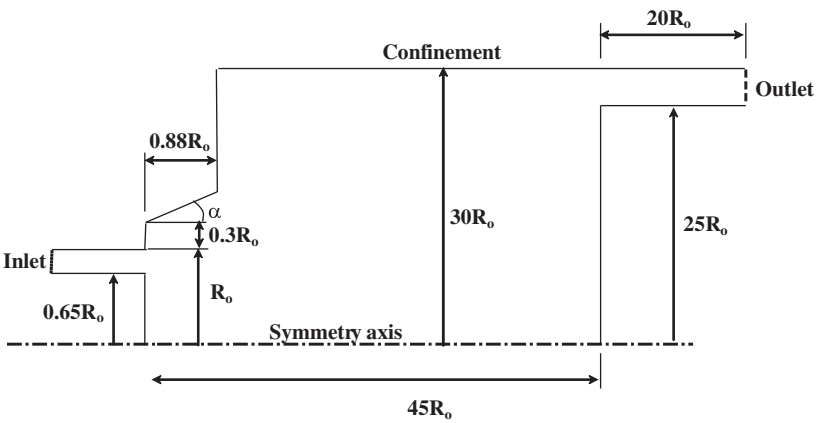

Figure 1. Schematic view of the geometry and computational domain.

DOI: 10.1002/fld

2.3. Inlet and boundary conditions

Previous studies revealed the importance to apply measured velocity profiles at the inlet in order to get accurate results in the velocity profiles when compared with experiments [13–15]. The goal of this paper is, however, to test the influence of the inlet velocity profile on the transitional swirl numbers. Therefore, two different inlets are chosen: one at $x = -7R_o$ (inlet 1) and another at $x = -0.11R_o$ downstream of the nozzle (inlet 2). The axial position of inlet 1 is determined based on the dimensions of the annular channel in the experimental set-up and the axial position of inlet 2 is determined based upon LDA measurements at that location to calibrate the swirl generator [3]. At inlet 1 a constant axial velocity of 6.48 m/s is applied. The azimuthal velocity profile is a solid body rotation, $W = \Omega R$, where Ω varies from 0 to 300 rad/s. At inlet 2 the measured LDA velocity profile from the experiments is applied. The Reynolds number based on the mean axial velocity and the difference in diameter of the annular channel $D_o - D_i$ is in both cases 10 650. The level of swirl is represented by the swirl number S, which is defined as the ratio of axial flux of azimuthal momentum to axial flux of axial momentum and outer radius,

$$S = \frac{\int_{R_i}^{R_o} 2\pi\rho U W r^2 \, dr}{R_o \int_{R_i}^{R_o} 2\pi\rho U^2 r \, dr} \tag{7}$$

Comparison of both inlet configurations is based on S by numerical integration of Equation (7). The range of swirl numbers investigated varies from 0 to 0.9. In case of the k–ε turbulence model the values of k and ε at both inlets are determined based on the turbulence intensity I and the hydraulic diameter of the annular channel D_H, $k = 3/2(UI)^2$ and $\varepsilon = C_\mu^{3/4} k^{3/2}/0.07D_H$, where U is the mean axial velocity in the channel and I is determined based on the experiments. For the Reynolds stress turbulence model (RSTM), the Reynolds stresses at the inlet are computed based on k using the assumption of isotropy of turbulence, $\overline{u^2} = \overline{v^2} = \overline{w^2} = \frac{2}{3}k$ and $\overline{uv} = \overline{uw} = \overline{vw} = 0$. The swirl generator used in the experimental set-up generates a flow which approximates very well these assumptions.

The modelling of swirling flows is a difficult task which is mainly due to two reasons. The first one is numerical: at high swirl numbers there is a strong coupling between the momentum equations due to the azimuthal velocity component. This results in large computational times. Also high gradients occur in a swirling flow which require a fine mesh and this also increases computational time. The second one is physical: highly swirling flow can have large recirculation zones meaning that downstream influences can be transported upstream [16, 17]. Therefore, one has to be very careful in choosing the right boundary conditions, especially at the outlet. In this case the experimental jet is a free jet. To simulate this, a confinement is placed at a radial distance of 30 times R_o. This dimension is chosen from a series of simulations and these have shown that placing the confinement there has no influence on the jet in the region of interest. Also the outlet position is chosen in this way at 65 times R_o. Usually for highly swirling flows, the experimentally measured velocity profile is applied at the outlet. In this case, this is not done for two reasons. First, the velocity profile could affect the transitional swirl numbers and second, we want to be sure that the swirl numbers where hysteresis occurs have exactly the same boundary conditions. To prevent the inflow through the outlet, it is partially blocked by a wall of length $25R_o$ at $x = 45R_o$ followed by a channel of length $20R_o$ to prevent the inflow in all cases. This is mainly done for increasing the computational speed. Varied simulations on the blocking ratio shows that this also has no influence on the jet. At the remainder of the outlet, Neumann boundary conditions for

DOI: 10.1002/fld

the variables are applied together with the radial pressure equilibrium, giving $\partial p/\partial r = \rho w^2/r$ at the outlet. A symmetry boundary condition is applied at the central axis. At the walls a no slip boundary conditions is applied. The mesh near the wall is fine enough to resolve the velocity profile near the wall. The first grid point in the normal direction to the wall is well inside the viscous sublayer resulting in a maximum y^+ of 3.

2.4. Solution strategy

Equations (1) and (2) together with the turbulence equations are solved using the finite volume-based solver Fluent 6.2 [18]. The momentum and turbulence equations are discretized using the third-order MUSCL differential scheme which improves spatial accuracy by reducing numerical diffusion compared with second-order upwind schemes [19]. The SIMPLEC algorithm is used for pressure–velocity coupling [20] and the pressure interpolation scheme is the PRESTO!-scheme [21]. The convergence criterion is based on the sum of the absolute values of the mass flow residual in each cell. The solution has converged when this sum is smaller than 1×10^{-8} kg/s.

2.5. Grid refinement study

A grid study was performed for two different swirl numbers: the zero swirl and the maximum swirl case. Two grids were taken: one coarse grid having 60 600 cells and another fine grid having 242 400 cells which is 4 times larger than the coarse one. Comparing the variables of the two grids shows that the maximum relative difference between the coarse and the fine grid is within 0.5%. Therefore, the coarse grid is already fine enough and the solution is grid independent.

3. RESULTS AND DISCUSSION

3.1. Flow structures

The first flow structure observed at zero swirl is called the 'closed jet flow' (CJF). The mean axial velocity profiles of a CJF are shown in Figure 2. Only the cases where the measured

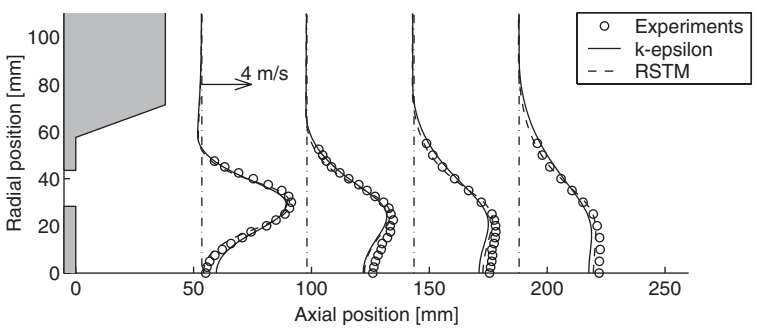

Figure 2. Experimental and numerical axial velocity profiles for the 'closed jet flow' at zero swirl. Only the calculations with the measured velocity profiles at the inlet are shown. The dashed-dotted line is the zero velocity line.

DOI: 10.1002/fld

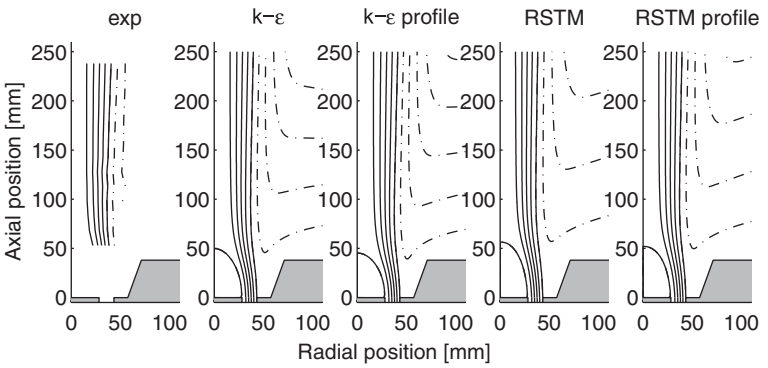

Figure 3. Experimental and numerical streamlines for the 'closed jet flow'. The solid lines indicate streamlines of the jet ($0 \leqslant \Psi \leqslant 1$) and the dashed-dotted lines indicate recirculation streamlines ($\Psi < 0$ or $\Psi > 1$).

velocity profile by LDA is applied at the inlet are shown in order to not overload the figure. Both the k–ε and the RSTMs predict the velocity profiles quite well. The RSTM predicts more accurately the velocity recovery in the wake of the central cylinder and also the velocity profile in the shear layer with the surroundings.

The iso-surface intersections of the $\theta = 0$ plane with the normalized stream function $\Psi(x, r, \theta) = \int_0^r ur\,\mathrm{d}r / \int_0^{D/2} ur\,\mathrm{d}r$ of a CJF are shown in Figure 3. The real streamlines of the flow are lines along the iso-surfaces of Ψ. The boundaries of the jet are given by $\Psi = 0$ (inner boundary) and $\Psi = 1$ (outer boundary). In total four different cases are shown: the standard k–ε model with an uniform axial and a solid body rotation for the azimuthal velocity at inlet 1 (k–ε), the standard k–ε model with the measured velocity profile by LDA applied at inlet 2 (k–ε profile), the RSTM with an uniform axial and a solid body rotation for the azimuthal velocity at inlet 1 (RSTM) and the RSTM with the measured velocity profile by LDA applied at inlet 2 (RSTM profile). The iso-surfaces plotted have the same values in all the five cases. Due to optical access the lowest axial position where LDA measurements are taken is $x = 53$ mm. Figure 3 shows that the streamlines in all cases are very similar. The stagnation point of the recirculation zone behind the central cylinder is the intersection of the central axis with the inner boundary of the jet ($\Psi = 0$). The velocity profile at the inlet has some influence on the axial location of this stagnation point. The outer boundary of the jet ($\Psi = 0$) is very similar for all the investigated cases.

Increasing the swirl induces an azimuthal velocity component in the flow field. When the level of swirl is low there is not much influence on the axial and radial velocity field. However, when the azimuthal velocity increases, large pressure gradients are induced in the flow field and at a certain swirl number a region of backflow along the central axis is induced called 'vortex breakdown' [1]. The occurrence of vortex breakdown is the transition from a CJF to an 'open jet flow low swirl' (OJF-LS). The swirl number where this transition occurs is called the critical swirl number. The axial and azimuthal velocity profiles of an OJF-LS are shown in Figure 4. Only the cases with a measured velocity profile at the inlet are shown in order not to overload the figure. The RSTM predicts the velocity profiles better than the k–ε model which underpredicts the axial velocity at the centreline. However, the axial velocity recovery downstream is overpredicted by the k–ε model and underpredicted by the RSTM which is consistent with the results of Tsai *et al*. [22]. The

DOI: 10.1002/fld

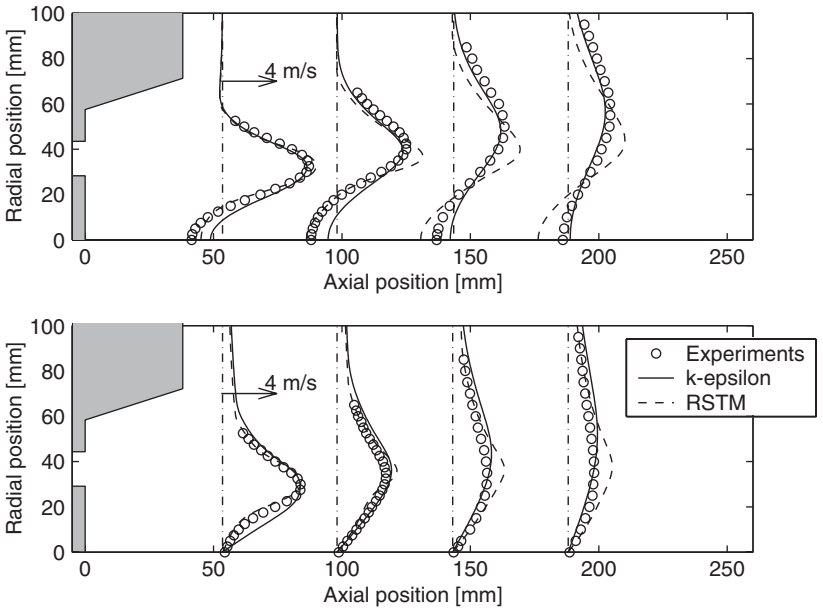

Figure 4. Experimental and numerical axial (top) and azimuthal (bottom) velocity profiles for the 'open jet flow low swirl' at $S = 0.56$. Only the calculations with the measured velocity profiles at the inlet are shown.

azimuthal velocity gradient at the central axis is better predicted by the RSTM model. However, the maximum azimuthal velocity is overpredicted and its decay in the downstream direction is underpredicted. In this swirl number regime a precessing vortex core (PVC) exists. The existence of the PVC is visible in a frequency analysis of the experimental LDA data [3]. This PVC is a 3D periodic motion in time which cannot be captured by the axisymmetric steady-state equations. The PVC also spatially averages the azimuthal velocity profile [23]. Therefore, the more diffusive nature of the k–ε model when compared with the RSTM model gives more accurate results for the maximum azimuthal velocity although for different physical reasons.

The streamlines for an OJF-LS are shown in Figure 5. The cases are the same as in Figure 3. Figure 5 shows that the inlet velocity profiles have a large influence on the velocity field as also found in literature [13–15]. In the experiments, the central vortex breakdown bubble closes. Only the k–ε model with the measured velocity profile at inlet 2 shows a fully closed bubble, the RSTM model with uniform axial velocity at inlet 1 shows a partially closed bubble and the other models show an open bubble. Due to the spatial averaging of the azimuthal velocity profile by the PVC, the pressure gradients in the radial direction are lowered. This azimuthal velocity field influences strongly the axial velocity field due to the strong coupling between the momentum equations. The RSTM model overpredicts the maximum azimuthal velocity and underpredicts it's decay and therefore overpredicts the subpressure in the centre and underpredicts its gradient in the downstream direction in comparison with the experiments. This underprediction of axial pressure gradient creates a larger bubble.

Further increasing the swirl leads to an increase in radial expansion of the jet. At a certain swirl number, the jet attaches to the divergent of the nozzle. This is the transition from an OJF-LS to

DOI: 10.1002/fld

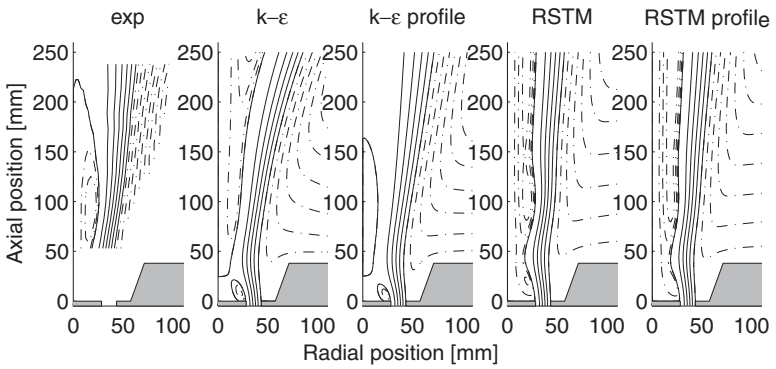

Figure 5. Experimental and numerical streamlines for the 'open jet flow low swirl' at $S = 0.56$. The solid lines indicate streamlines of the jet ($0 \leqslant \Psi \leqslant 1$) and the dashed-dotted lines indicate recirculation streamlines ($\Psi < 0$ or $\Psi > 1$).

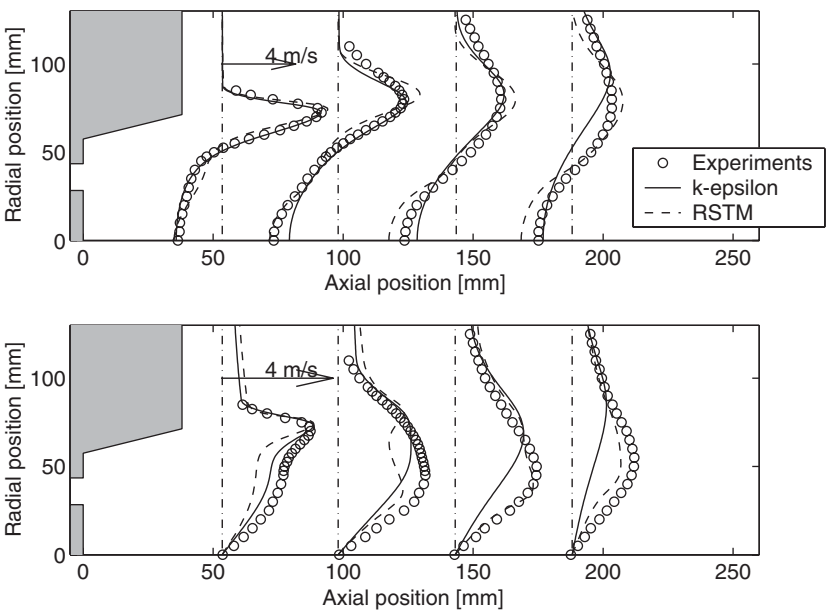

Figure 6. Experimental and numerical axial (top) and azimuthal (bottom) velocity profiles for the 'open jet flow high swirl' at $S = 0.904$. Only the calculations with the measured velocity profiles at the inlet are shown.

an 'open jet flow high swirl' (OJF-HS). The axial and azimuthal velocity fields of an OJF-HS are shown in Figure 6. Although the k–ε model is known to be not very accurate in highly swirling flows, the predictions near the nozzle of the azimuthal velocity is better than the RSTM predictions. Further downstream the RSTM model predicts both the axial and azimuthal velocity fields better than the k–ε model. This can also be seen when looking at the streamlines in Figure 7. The radial expansion of the jet is overpredicted in both cases of the k–ε model.

DOI: 10.1002/fld

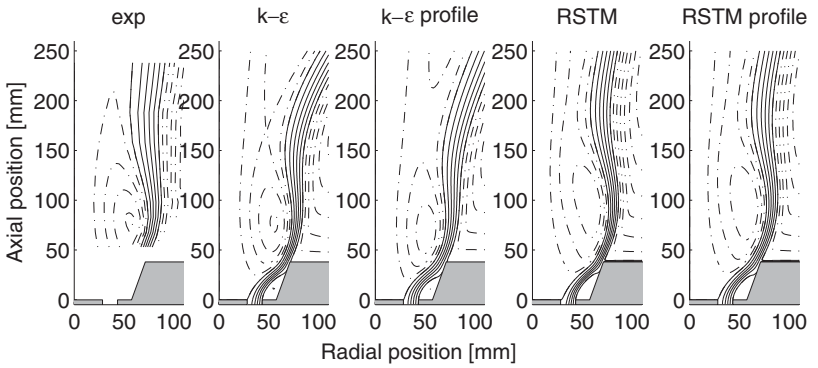

Figure 7. Experimental and numerical streamlines for the 'open jet flow high swirl' at $S = 0.904$. The solid lines indicate streamlines of the jet ($0 \leqslant \Psi \leqslant 1$) and the dashed-dotted lines indicate recirculation streamlines ($\Psi < 0$ or $\Psi > 1$).

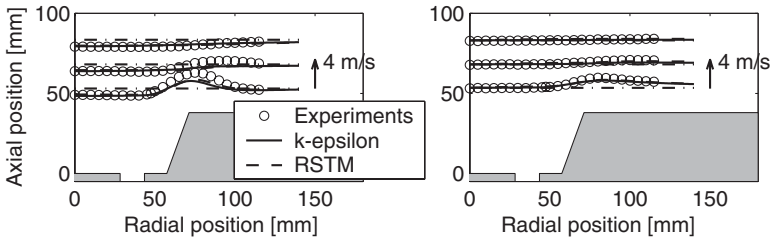

Figure 8. Experimental and numerical axial velocity profiles for the 'coanda jet flow' at $S = 0.56$. Only the calculations with the measured velocity profiles at the inlet are shown.

Starting at an OJF-HS and decreasing the swirl increases the radial expansion of the jet. Due to the increased radial expansion, the coanda effect takes place at the nozzle outlet and pulls the jet towards the wall of the nozzle outlet (Figure 8). This transition is the transition from an OJF-HS to a 'coanda jet flow' (CoJF). The CoJF creates a very uniform and low turbulent central downflow. The streamlines of a CoJF are shown in Figure 9.

3.2. Hysteresis

One cycle of starting at zero swirl and increasing the swirl till maximum and then decreasing the swirl back to zero generates four different jet patterns. Figure 10 shows the transition map for an increase and subsequent decrease in swirl. The starting point is the CJF at zero swirl. Increasing the swirl creates large pressure gradients in the axial direction which eventually lead to vortex breakdown. The critical swirl number where vortex breakdown takes place is underpredicted by both the RSTM models and overpredicted by the k–ε model. It is believed that the overprediction of the turbulent viscosity in the k–ε model suppresses the occurrence of the bubble [24]. It is also clear from the figure that the inlet velocity profile has no notable influence on the critical swirl number. The transitional swirl number from OJF-LS to OJF-HS is overpredicted by both models

DOI: 10.1002/fld

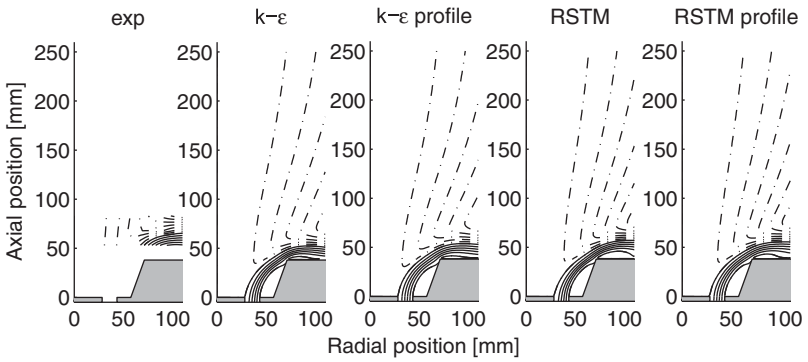

Figure 9. Experimental and numerical streamlines for the 'coanda jet flow' at $S = 0.56$. The solid lines indicate streamlines of the jet ($0 \leqslant \Psi \leqslant 1$) and the dashed-dotted lines indicate recirculation streamlines ($\Psi < 0$ or $\Psi > 1$).

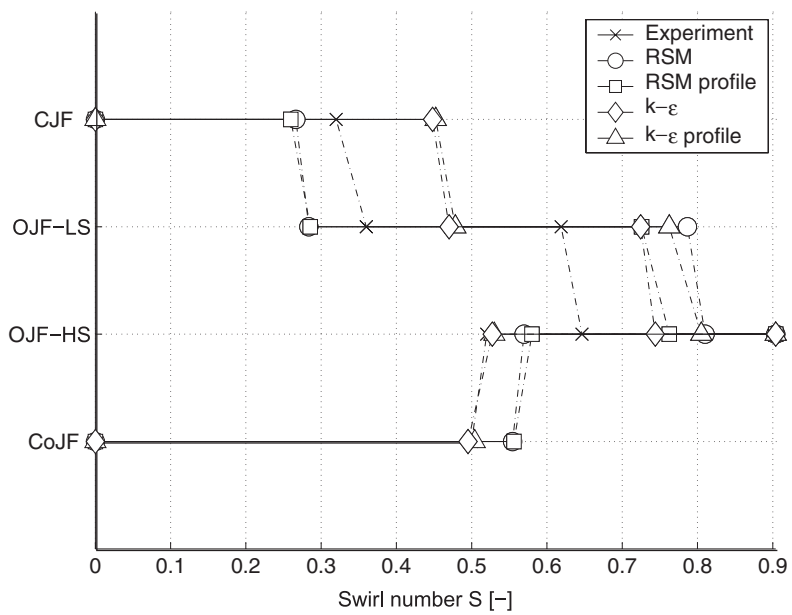

Figure 10. Transition map of a cycle increasing till maximum swirl followed by a decrease till zero swirl.

and for both inlet conditions. The inlet profiles have more influence than the turbulence models. Both the RSTM and the k–ε with the measured velocity profile at the inlet predict this transition better. The OJF-HS remains till maximum swirl. Starting at maximum swirl and decreasing the swirl increases the radial expansion of the jet. Due to the increased radial expansion the coanda effect takes place at the nozzle outlet and pulls the jet towards the wall of the nozzle outlet. This is the transition to a CoJF. The inlet velocity profiles do not have much influence on this transition.

DOI: 10.1002/fld

Since the k–ε model is known to be not very good at intermediate and high swirl numbers, it predicts this transitional swirl number surprisingly better than the RSTM model. The CoJF remains till zero swirl and this stability is predicted by all the models.

4. CONCLUDING REMARKS

A simulation of the hysteresis in annular swirling jets with a stepped-conical expansion nozzle has been performed using two turbulence models. Both turbulence models predict the four different existing flow structures. Also the hysteresis between the flow structures when increasing and subsequently decreasing the swirl is predicted correctly. The influence of the inlet conditions on the transitional swirl numbers is also investigated. Although the k–ε turbulence model is known to be not very accurate for highly swirling flows, it predicts the four flow structures, the transitional swirl numbers and the global hysteresis with the stability of the coanda flow to zero swirl.

REFERENCES

1. Gupta AK, Lilley DG, Syred N. *Swirl Flows*. Abacus Press: Tunbridge Wells, U.K., 1984.
2. Chedaille J, Leuckel W, Chesters AK. Aerodynamic studies carried out on turbulent jets by the international flame research foundation. *Journal of the Institute of Fuel* 1966; **39**(311):506–521.
3. Vanierschot M, Van den Bulck E. Multiple flow patterns in annular swirling jets. *Experimental Thermal and Fluid Science*, accepted. doi:10.1016/j.expthermflusci.2006.06.001.
4. Jiang TL, Shen CH. Numerical predictions of the bifurcation of confined swirling flows. *International Journal for Numerical Methods in Fluids* 1994; **19**:961–979.
5. Sloan DG, Smith PJ, Smoot LD. Modeling of swirl in turbulent flow systems. *Progress in Energy and Combustion Science* 1986; **12**:163–250.
6. Vanierschot M, Van den Bulck E. Influence of the nozzle geometry on the hysteresis of annular swirling jets. *Combustion Science and Technology*, accepted.
7. Vanoverberghe K, Van den Bulck E, Hubner W, Tummers M. Multiflame patterns in swirl-driven partially premixed natural combustion. *Transactions of the ASME*: *Journal of Engineering for Gas Turbines and Power* 2003; **125**:40–45.
8. Launder BE, Spalding DB. The numerical computation of turbulent flows. *Computer Methods in Applied Mechanics and Engineering* 1974; **3**(3):269–289.
9. Launder BE, Reece GJ, Rodi W. Progress in the development of a Reynolds stress turbulence closure. *Journal of Fluid Mechanics* 1975; **68**(3):537–566.
10. Gibson MM, Launder BE. Ground effects on pressure fluctuations in the atmospheric boundary layer. *Journal of Fluid Mechanics* 1978; **86**:491–511.
11. Daly BJ, Harlow FH. Transport equations in turbulence. *Physics of Fluids* 1970; **13**:2634–2649.
12. Lien FS, Leschziner MA. Assessment of turbulent transport models including non-linear RNG Eddy-viscosity formulation and second-moment closure. *Computers and Fluids* 1994; **23**(8):983–1004.
13. Ramos JI. Turbulent nonreacting swirling flows. *AIAA Journal* 1984; **22**(6):846–848.
14. Dong M, Lilley DG. Inlet velocity profile effects on turbulent swirling flow predictions. *Journal of Propulsion and Power* 1994; **10**(2):155–160.
15. Leschziner MA, Rodi W. Computation of strongly swirling axisymmetric free jets. *AIAA Journal* 1984; **22**(12):1742–1747.
16. Escudier MP, Bornstein J, Zehnder N. Observations and LDA measurements of confined turbulent vortex flow. *Journal of Fluid Mechanics* 1980; **98**(1):49–63.
17. Escudier MP, Keller JJ. Recirculation in swirling flow: a manifestation of vortex breakdown. *AIAA Journal* 1985; **23**:111–116.
18. *Fluent 6.2 User's guide.* Fluent Inc., January 2005.
19. Van Leer B. Toward the ultimate conservative difference scheme. IV. A second order sequel to Gudunov's method. *Journal of Computational Physics* 1979; **32**:101–136.

DOI: 10.1002/fld

20. Vandoormaal JP, Raithby GD. Enhancements of the SIMPLE method for predicting incompressible fluid flows. *Numerical Heat Transfer* 1984; **7**:147–163.
21. Pantakar SV. *Numerical Heat Transfer and Fluid Flow*. Hemisphere: Washington, DC, 1980.
22. Tsai JH, Lin CA, Lu CM. Modelling dump combustor flows with and without swirl at the inlet using Reynolds stress models. *International Journal for Numerical Methods in Heat and Fluid Flow* 1995; **5**:577–588.
23. Hoekstra AJ, Derksen JJ, Van Den Akker HEA. An experimental and numerical study of turbulent swirling flow in gas cyclones. *Chemical Engineering Science* 1999; **54**:2055–2065.
24. Lai YG. Predictive capabilities of turbulence models for a confined swirling flow. *AIAA Journal* 1995; **34**(8): 1743–1745.

DOI: 10.1002/fld